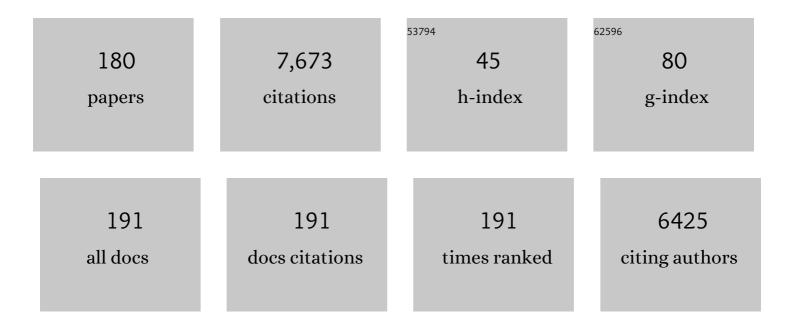
Zhenhong Li

List of Publications by Year in descending order

Source: https://exaly.com/author-pdf/9578645/publications.pdf Version: 2024-02-01



ZHENHONGL

#	Article	IF	CITATIONS
1	Precision agriculture technology adoption: a qualitative study of small-scale commercial "family farms―located in the North China Plain. Precision Agriculture, 2022, 23, 319-351.	6.0	30
2	Coseismic and postseismic deformation of the 2016 Mw 6.0 Petermann ranges earthquake from satellite radar observations. Advances in Space Research, 2022, 69, 376-385.	2.6	8
3	Identifying barriers to sustainable apple production: A stakeholder perspective. Journal of Environmental Management, 2022, 302, 114082.	7.8	17
4	Quantifying the influence of long-term overexploitation on deep groundwater resources across Cangzhou in the North China Plain using InSAR measurements. Journal of Hydrology, 2022, 605, 127368.	5.4	28
5	Time-Varying Surface Deformation Retrieval and Prediction in Closed Mines through Integration of SBAS InSAR Measurements and LSTM Algorithm. Remote Sensing, 2022, 14, 788.	4.0	13
6	New insights into the 2020 Sardoba dam failure in Uzbekistan from Earth observation. International Journal of Applied Earth Observation and Geoinformation, 2022, 107, 102705.	2.8	25
7	Geospatial Transformer Is What You Need for Aircraft Detection in SAR Imagery. IEEE Transactions on Geoscience and Remote Sensing, 2022, 60, 1-15.	6.3	7
8	Mapping Tidal Flats of the Bohai and Yellow Seas Using Time Series Sentinel-2 Images and Google Earth Engine. Remote Sensing, 2022, 14, 1789.	4.0	14
9	Comparison and transferability of thermal, temporal and phenological-based in-season predictions of above-ground biomass in wheat crops from proximal crop reflectance data. Remote Sensing of Environment, 2022, 273, 112967.	11.0	41
10	Surface Deformation of Expansive Soil at Ankang Airport, China, Revealed by InSAR Observations. Remote Sensing, 2022, 14, 2217.	4.0	8
11	Reconstructing of High-Spatial-Resolution Three-Dimensional Electron Density by Ingesting SAR-Derived VTEC Into IRI Model. IEEE Geoscience and Remote Sensing Letters, 2022, 19, 1-5.	3.1	24
12	Spatiotemporal Change Detection of Coastal Wetlands Using Multi-Band SAR Coherence and Synergetic Classification. Remote Sensing, 2022, 14, 2610.	4.0	6
13	ä€ç§åŸºäºŽåቖæ•饿"Ÿçš"æ»'åŧé~²ç³⁄4技æœ⁻框架åŠå…¶å·¥ç¨‹åº"用. Diqiu Kexue - Zhongguo Dizhi Daxue . Geosciences, 2022, 47, 1901.	Xuebao/Ea 0.5	arth ₄ Science - J
14	å•è—ë°≇€šå»Šé"æž—æ³¢æ®µå†°å•æ³¥çŸ³æµå'è,²åŠ¨æ€æ¼'"化å^†æžåŠç›'测预è∤æ–¹æj^. Diqiu Kexue - Zh Geosciences, 2022, 47, 1969.	ongguo D	izhi Daxue Xu
15	A New Coherence Detection Method for Mapping Inland Water Bodies Using CYGNSS Data. Remote Sensing, 2022, 14, 3195.	4.0	7
16	Recognition of the coastal dune migration micro-deformation in Changli Gold Coast of China based on GB-InSAR. Marine Georesources and Geotechnology, 2021, 39, 747-755.	2.1	1
17	Iterative-SGLRT for Multiple-Scatterer Detection in SAR Tomography. IEEE Geoscience and Remote Sensing Letters, 2021, 18, 122-126.	3.1	4
18	A new agricultural drought index for monitoring the water stress of winter wheat. Agricultural Water Management, 2021, 244, 106599.	5.6	21

#	Article	IF	CITATIONS
19	Lake Level Change From Satellite Altimetry Over Seasonally Ice-Covered Lakes in the Mackenzie River Basin. IEEE Transactions on Geoscience and Remote Sensing, 2021, 59, 8143-8152.	6.3	6
20	Reconstruction and Evaluation of DEMs From Bistatic Tandem-X SAR in Mountainous and Coastal Areas of China. IEEE Journal of Selected Topics in Applied Earth Observations and Remote Sensing, 2021, 14, 5152-5170.	4.9	7
21	Use of Google Earth Engine to Generate a 20-Year 1 Km × 1 Km Monthly Air Temperature Product Over Yellow River Basin. IEEE Journal of Selected Topics in Applied Earth Observations and Remote Sensing, 2021, 14, 10079-10090.	4.9	3
22	Improved Estimation of Winter Wheat Aboveground Biomass Using Multiscale Textures Extracted from UAV-Based Digital Images and Hyperspectral Feature Analysis. Remote Sensing, 2021, 13, 581.	4.0	56
23	Wide Sliding Window and Subsampling Network for Hyperspectral Image Classification. Remote Sensing, 2021, 13, 1290.	4.0	7
24	Statistical assessment metrics for InSAR atmospheric correction: Applications to generic atmospheric correction online service for InSAR (GACOS) in Eastern China. International Journal of Applied Earth Observation and Geoinformation, 2021, 96, 102289.	2.8	17
25	Landslide geometry and activity in Villa de la Independencia (Bolivia) revealed by InSAR and seismic noise measurements. Landslides, 2021, 18, 2721-2737.	5.4	13
26	Integration of Sentinel-1 and ALOS/PALSAR-2 SAR datasets for mapping active landslides along the Jinsha River corridor, China. Engineering Geology, 2021, 284, 106033.	6.3	88
27	Watch Out for the Tailings Pond, a Sharp Edge Hanging over Our Heads: Lessons Learned and Perceptions from the Brumadinho Tailings Dam Failure Disaster. Remote Sensing, 2021, 13, 1775.	4.0	24
28	Global Comparisons of ERA5 and the Operational HRES Tropospheric Delay and Water Vapor Products With GPS and MODIS. Earth and Space Science, 2021, 8, e2020EA001417.	2.6	22
29	Spatiotemporal Changes of Coastline over the Yellow River Delta in the Previous 40 Years with Optical and SAR Remote Sensing. Remote Sensing, 2021, 13, 1940.	4.0	26
30	Retrieving Three-Dimensional Large Surface Displacements in Coal Mining Areas by Combining SAR Pixel Offset Measurements with an Improved Mining Subsidence Model. Remote Sensing, 2021, 13, 2541.	4.0	14
31	Geodetic Constraints on Recent Subduction Earthquakes and Future Seismic Hazards in the Southwestern Coast of Mexico. Geophysical Research Letters, 2021, 48, e2021GL094192.	4.0	2
32	Dynamic Wide and Deep Neural Network for Hyperspectral Image Classification. Remote Sensing, 2021, 13, 2575.	4.0	7
33	Landslide Detection in the Linzhi–Ya'an Section along the Sichuan–Tibet Railway Based on InSAR and Hot Spot Analysis Methods. Remote Sensing, 2021, 13, 3566.	4.0	29
34	Employing deep learning for automatic river bridge detection from SAR images based on Adaptively effective feature fusion. International Journal of Applied Earth Observation and Geoinformation, 2021, 102, 102425.	2.8	9
35	Phase unmixing of TerraSAR-X staring spotlight interferograms in building scale for PS height and deformation. ISPRS Journal of Photogrammetry and Remote Sensing, 2021, 180, 14-28.	11.1	2
36	Synergetic Classification of Coastal Wetlands over the Yellow River Delta with GF-3 Full-Polarization SAR and Zhuhai-1 OHS Hyperspectral Remote Sensing. Remote Sensing, 2021, 13, 4444.	4.0	18

#	Article	IF	CITATIONS
37	Simulating the Response of the Surface Urban Heat Environment to Land Use and Land Cover Changes: A Case Study of Wuhan, China. Remote Sensing, 2021, 13, 4495.	4.0	5
38	Using CYGNSS Data to Map Flood Inundation during the 2021 Extreme Precipitation in Henan Province, China. Remote Sensing, 2021, 13, 5181.	4.0	30
39	Sequential Estimation of Dynamic Deformation Parameters for SBAS-InSAR. IEEE Geoscience and Remote Sensing Letters, 2020, 17, 1017-1021.	3.1	20
40	A New Baseline Linear Combination Algorithm for Generating Urban Digital Elevation Models With Multitemporal InSAR Observations. IEEE Transactions on Geoscience and Remote Sensing, 2020, 58, 1120-1133.	6.3	14
41	The 2018 <i>M</i> _{<i>w</i>} 7.5 Papua New Guinea Earthquake: A Possible Complex Multiple Faults Failure Event With Deepâ€eated Reverse Faulting. Earth and Space Science, 2020, 7, e2019EA000966.	2.6	13
42	A hierarchical interannual wheat yield and grain protein prediction model using spectral vegetative indices and meteorological data. Field Crops Research, 2020, 248, 107711.	5.1	40
43	Joint Inversion of Geodetic Observations and Relative Weighting—The 1999 Mw 7.6 Chi-Chi Earthquake Revisited. Remote Sensing, 2020, 12, 3125.	4.0	2
44	Triggered afterslip on the southern Hikurangi subduction interface following the 2016 KaikÅura earthquake from InSAR time series with atmospheric corrections. Remote Sensing of Environment, 2020, 251, 112097.	11.0	41
45	Highâ€Resolution Surface Velocities and Strain for Anatolia From Sentinelâ€1 InSAR and GNSS Data. Geophysical Research Letters, 2020, 47, e2020GL087376.	4.0	108
46	UAV-Based Photogrammetry and LiDAR for the Characterization of Ice Morphology Evolution. IEEE Journal of Selected Topics in Applied Earth Observations and Remote Sensing, 2020, 13, 4188-4199.	4.9	19
47	Ocean Tide Loading Effects on InSAR Observations Over Wide Regions. Geophysical Research Letters, 2020, 47, e2020GL088184.	4.0	12
48	Coastal Dam Inundation Assessment for the Yellow River Delta: Measurements, Analysis and Scenario. Remote Sensing, 2020, 12, 3658.	4.0	24
49	Winter Wheat Nitrogen Status Estimation Using UAV-Based RCB Imagery and Gaussian Processes Regression. Remote Sensing, 2020, 12, 3778.	4.0	46
50	Quantifying Ground Subsidence Associated with Aquifer Overexploitation Using Space-Borne Radar Interferometry in Kabul, Afghanistan. Remote Sensing, 2020, 12, 2461.	4.0	14
51	Optimizing Global Navigation Satellite Systems network real-time kinematic infrastructure for homogeneous positioning performance from the perspective of tropospheric effects. Proceedings of the Royal Society A: Mathematical, Physical and Engineering Sciences, 2020, 476, 20200248.	2.1	2
52	Geospatial Contextual Attention Mechanism for Automatic and Fast Airport Detection in SAR Imagery. IEEE Access, 2020, 8, 173627-173640.	4.2	12
53	A Multi-Scale Deep Neural Network for Water Detection from SAR Images in the Mountainous Areas. Remote Sensing, 2020, 12, 3205.	4.0	16
54	Effects of Agricultural Cooperative Society on Farmers' Technical Efficiency: Evidence from Stochastic Frontier Analysis. Sustainability, 2020, 12, 8194.	3.2	14

#	Article	IF	CITATIONS
55	A hybrid modelling approach to understanding adoption of precision agriculture technologies in Chinese cropping systems. Computers and Electronics in Agriculture, 2020, 172, 105305.	7.7	52
56	Measuring the Urban Land Surface Temperature Variations Under Zhengzhou City Expansion Using Landsat-Like Data. Remote Sensing, 2020, 12, 801.	4.0	20
57	Three-dimensional time-varying large surface displacements in coal exploiting areas revealed through integration of SAR pixel offset measurements and mining subsidence model. Remote Sensing of Environment, 2020, 240, 111663.	11.0	52
58	Entering the Era of Earth Observation-Based Landslide Warning Systems: A Novel and Exciting Framework. IEEE Geoscience and Remote Sensing Magazine, 2020, 8, 136-153.	9.6	90
59	Deformation of the Baige Landslide, Tibet, China, Revealed Through the Integration of Crossâ€Platform ALOS/PALSARâ€1 and ALOS/PALSARâ€2 SAR Observations. Geophysical Research Letters, 2020, 47, e2019GL086142.	4.0	36
60	Diagnosing Subsidence Geohazard at Beijing Capital International Airport, from High-Resolution SAR Interferometry. Sustainability, 2020, 12, 2269.	3.2	14
61	Progress of hyperspectral data processing and modelling for cereal crop nitrogen monitoring. Computers and Electronics in Agriculture, 2020, 172, 105321.	7.7	26
62	In-season biomass estimation of oilseed rape (Brassica napus L.) using fully polarimetric SAR imagery. Precision Agriculture, 2019, 20, 630-648.	6.0	19
63	Super-Resolved Multiple Scatterers Detection in SAR Tomography Based on Compressive Sensing Generalized Likelihood Ratio Test (CS-GLRT). Remote Sensing, 2019, 11, 1930.	4.0	12
64	A New Processing Chain for Real-Time Ground-Based SAR (RT-GBSAR) Deformation Monitoring. Remote Sensing, 2019, 11, 2437.	4.0	8
65	InSAR Time Series Analysis of L-Band Data for Understanding Tropical Peatland Degradation and Restoration. Remote Sensing, 2019, 11, 2592.	4.0	15
66	Modelling of instrument repositioning errors in discontinuous Multi-Campaign Ground-Based SAR (MC-GBSAR) deformation monitoring. ISPRS Journal of Photogrammetry and Remote Sensing, 2019, 157, 26-40.	11.1	15
67	Crop Water Content of Winter Wheat Revealed with Sentinel-1 and Sentinel-2 Imagery. Sensors, 2019, 19, 4013.	3.8	30
68	Automatic Extraction of Water and Shadow from SAR Images Based on a Multi-Resolution Dense Encoder and Decoder Network. Sensors, 2019, 19, 3576.	3.8	27
69	Land subsidence in Beijing and its relationship with geological faults revealed by Sentinel-1 InSAR observations. International Journal of Applied Earth Observation and Geoinformation, 2019, 82, 101886.	2.8	53
70	Copula-Based Drought Analysis Using Standardized Precipitation Evapotranspiration Index: A Case Study in the Yellow River Basin, China. Water (Switzerland), 2019, 11, 1298.	2.7	23
71	A New Deep Learning Algorithm for SAR Scene Classification Based on Spatial Statistical Modeling and Features Re-Calibration. Sensors, 2019, 19, 2479.	3.8	19
72	Multi-LUTs method for canopy nitrogen density estimation in winter wheat by field and UAV hyperspectral. Computers and Electronics in Agriculture, 2019, 162, 174-182.	7.7	55

#	Article	IF	CITATIONS
73	Deformation Monitoring of Reservoir Dams Using GNSS: An Application to South-to-North Water Diversion Project, China. IEEE Access, 2019, 7, 54981-54992.	4.2	48
74	Drought Evaluation with CMORPH Satellite Precipitation Data in the Yellow River Basin by Using Gridded Standardized Precipitation Evapotranspiration Index. Remote Sensing, 2019, 11, 485.	4.0	39
75	A Combined Quantitative Evaluation Model for the Capability of Hyperspectral Imagery for Mineral Mapping. Sensors, 2019, 19, 328.	3.8	5
76	Resolving Fine-Scale Surface Features on Polar Sea Ice: A First Assessment of UAS Photogrammetry Without Ground Control. Remote Sensing, 2019, 11, 784.	4.0	25
77	Post-disaster assessment of 2017 catastrophic Xinmo landslide (China) by spaceborne SAR interferometry. Landslides, 2019, 16, 1189-1199.	5.4	36
78	Coseismic Slip Distribution of the 2019 Mw 7.5 New Ireland Earthquake from the Integration of Multiple Remote Sensing Techniques. Remote Sensing, 2019, 11, 2767.	4.0	5
79	Integration of Range Split Spectrum Interferometry and conventional InSAR to monitor large gradient surface displacements. International Journal of Applied Earth Observation and Geoinformation, 2019, 74, 130-137.	2.8	9
80	Source parameters of the 2017 <i>M</i> w 6.2 Yukon earthquake doublet inferred from coseismic GPS and ALOS-2 deformation measurements. Geophysical Journal International, 2019, 216, 1517-1528.	2.4	12
81	A comparative review of the state and advancement of Site-Specific Crop Management in the UK and China. Frontiers of Agricultural Science and Engineering, 2019, 6, 116.	1.4	9
82	Multi-GNSS precise point positioning for precision agriculture. Precision Agriculture, 2018, 19, 895-911.	6.0	69
83	Distribution and characteristics of loess landslides triggered by the 1920 Haiyuan Earthquake, Northwest of China. Geomorphology, 2018, 314, 1-12.	2.6	67
84	Interferometric synthetic aperture radar atmospheric correction using a GPS-based iterative tropospheric decomposition model. Remote Sensing of Environment, 2018, 204, 109-121.	11.0	237
85	New Approaches to Processing Ground-based SAR (GBSAR) Data for Deformation Monitoring. Remote Sensing, 2018, 10, 1936.	4.0	7
86	Capability of Remotely Sensed Drought Indices for Representing the Spatio–Temporal Variations of the Meteorological Droughts in the Yellow River Basin. Remote Sensing, 2018, 10, 1834.	4.0	37
87	Three-dimensional (3D) morphology of Sansha Yongle Blue Hole in the South China Sea revealed by underwater remotely operated vehicle. Scientific Reports, 2018, 8, 17122.	3.3	17
88	Remote Sensing of Leaf and Canopy Nitrogen Status in Winter Wheat (Triticum aestivum L.) Based on N-PROSAIL Model. Remote Sensing, 2018, 10, 1463.	4.0	38
89	ISBDD Model for Classification of Hyperspectral Remote Sensing Imagery. Sensors, 2018, 18, 780.	3.8	0
90	Predicting Grain Protein Content in Winter Wheat Using Hyperspectral and Meteorological Factor. , 2018, , .		1

6

#	Article	IF	CITATIONS
91	Evaluation of the Stability of the Darbandikhan Dam after the 12 November 2017 Mw 7.3 Sarpol-e Zahab (Iran–Iraq Border) Earthquake. Remote Sensing, 2018, 10, 1426.	4.0	19
92	Generic Atmospheric Correction Model for Interferometric Synthetic Aperture Radar Observations. Journal of Geophysical Research: Solid Earth, 2018, 123, 9202-9222.	3.4	326
93	Estimating genetic parameters of DSSAT-CERES model with the GLUE method for winter wheat (Triticum aestivum L.) production. Computers and Electronics in Agriculture, 2018, 154, 213-221.	7.7	50
94	Monitoring Highway Stability in Permafrost Regions with X-band Temporary Scatterers Stacking InSAR. Sensors, 2018, 18, 1876.	3.8	37
95	Resolving Surface Displacements in Shenzhen of China from Time Series InSAR. Remote Sensing, 2018, 10, 1162.	4.0	26
96	Small Magnitude Co-Seismic Deformation of the 2017 Mw 6.4 Nyingchi Earthquake Revealed by InSAR Measurements with Atmospheric Correction. Remote Sensing, 2018, 10, 684.	4.0	20
97	Dual control of fault intersections on stop-start rupture in the 2016 Central Italy seismic sequence. Earth and Planetary Science Letters, 2018, 500, 1-14.	4.4	100
98	A New Nonlocal Method for Ground-Based Synthetic Aperture Radar Deformation Monitoring. IEEE Journal of Selected Topics in Applied Earth Observations and Remote Sensing, 2018, 11, 3769-3781.	4.9	8
99	A new approach to selecting coherent pixels for ground-based SAR deformation monitoring. ISPRS Journal of Photogrammetry and Remote Sensing, 2018, 144, 412-422.	11.1	25
100	A proposed framework for accelerating technology trajectories in agriculture: a case study in China. Frontiers of Agricultural Science and Engineering, 2018, .	1.4	13
101	Source characteristics of the 2015 MW 7.8 Gorkha (Nepal) earthquake and its MW 7.2 aftershock from space geodesy. Tectonophysics, 2017, 712-713, 747-758.	2.2	43
102	Generation of realâ€time mode highâ€resolution water vapor fields from GPS observations. Journal of Geophysical Research D: Atmospheres, 2017, 122, 2008-2025.	3.3	182
103	Land subsidence prediction in Beijing based on PS-InSAR technique and improved Grey-Markov model. GIScience and Remote Sensing, 2017, 54, 797-818.	5.9	51
104	Probing Coulomb stress triggering effects for a Mw > 6.0 earthquake sequence from 1997 to 2014 along the periphery of the Bayan Har block on the Tibetan Plateau. Tectonophysics, 2017, 694, 249-267.	2.2	14
105	Unmanned Aerial Vehicle Remote Sensing for Field-Based Crop Phenotyping: Current Status and Perspectives. Frontiers in Plant Science, 2017, 8, 1111.	3.6	448
106	Earth Observations for Geohazards: Present and Future Challenges. Remote Sensing, 2017, 9, 194.	4.0	46
107	A Flexible, Generic Photogrammetric Approach to Zoom Lens Calibration. Remote Sensing, 2017, 9, 244.	4.0	6
108	Landslide Susceptibility Mapping Using GIS-based Vector Grid File (VGF) Validating with InSAR Techniques: Three Gorges, Yangtze River (China). AIMS Geosciences, 2017, 3, 116-141.	1.0	4

#	Article	IF	CITATIONS
109	Estimation of winter wheat canopy nitrogen density at different growth stages based on Multi-LUT approach. , 2017, , .		0
110	Imaging Land Subsidence Induced by Groundwater Extraction in Beijing (China) Using Satellite Radar Interferometry. Remote Sensing, 2016, 8, 468.	4.0	142
111	Potassium and Obesity/Metabolic Syndrome: A Systematic Review and Meta-Analysis of the Epidemiological Evidence. Nutrients, 2016, 8, 183.	4.1	64
112	Anatomy of Subsidence in Tianjin from Time Series InSAR. Remote Sensing, 2016, 8, 266.	4.0	33
113	Time-Dependent Afterslip of the 2009 Mw 6.3 Dachaidan Earthquake (China) and Viscosity beneath the Qaidam Basin Inferred from Postseismic Deformation Observations. Remote Sensing, 2016, 8, 649.	4.0	11
114	New Advances on Environment Monitoring with Wireless Sensor Network. International Journal of Distributed Sensor Networks, 2016, 12, 2378070.	2.2	2
115	GNSS tropospheric gradients with high temporal resolution and their effect on precise positioning. Journal of Geophysical Research D: Atmospheres, 2016, 121, 912-930.	3.3	30
116	Monitoring peat subsidence and carbon emission in Indonesia peatlands using InSAR time series. , 2016, , .		4
117	Measurement of subsidence in the Yangbajing geothermal fields, Tibet, from TerraSAR-X InSAR time series analysis. International Journal of Digital Earth, 2016, 9, 697-709.	3.9	25
118	Short-term effects of atmospheric particulate matter on myocardial infarction: a cumulative meta-analysis. Environmental Science and Pollution Research, 2016, 23, 6139-6148.	5.3	32
119	A new quality validation of global digital elevation models freely available in China. Survey Review, 2016, 48, 409-420.	1.2	13
120	Monitoring activity at the Daguangbao mega-landslide (China) using Sentinel-1 TOPS time series interferometry. Remote Sensing of Environment, 2016, 186, 501-513.	11.0	145
121	Biomass estimation of oilseed rape using simulated compact polarimtric SAR imagery. , 2016, , .		3
122	Using wavelet tools to analyse seasonal variations from InSAR time-series data: a case study of the Huangtupo landslide. Landslides, 2016, 13, 437-450.	5.4	99
123	State-of-the-art in studies of glacial isostatic adjustment for the British Isles: a literature review. Earth and Environmental Science Transactions of the Royal Society of Edinburgh, 2015, 106, 145-170.	0.3	7
124	Land Subsidence over Oilfields in the Yellow River Delta. Remote Sensing, 2015, 7, 1540-1564.	4.0	29
125	Extracting Vertical Displacement Rates in Shanghai (China) with Multi-Platform SAR Images. Remote Sensing, 2015, 7, 9542-9562.	4.0	62
126	High interseismic coupling in the Eastern Makran (Pakistan) subduction zone. Earth and Planetary Science Letters, 2015, 420, 116-126.	4.4	24

#	Article	IF	CITATIONS
127	Random Forest and Rotation Forest for fully polarized SAR image classification using polarimetric and spatial features. ISPRS Journal of Photogrammetry and Remote Sensing, 2015, 105, 38-53.	11.1	357
128	Spatiotemporal characteristics of the Huangtupo landslide in the Three Gorges region (China) constrained by radar interferometry. Geophysical Journal International, 2014, 197, 213-232.	2.4	54
129	Sensitivity of Coulomb stress change to the parameters of the Coulomb failure model: A case study using the 2008 <i>M_w</i> 7.9 Wenchuan earthquake. Journal of Geophysical Research: Solid Earth, 2014, 119, 3371-3392.	3.4	40
130	Patterns and mechanisms of coseismic and postseismic slips of the 2011 M W 7.1 Van (Turkey) earthquake revealed by multi-platform synthetic aperture radar interferometry. Tectonophysics, 2014, 632, 188-198.	2.2	32
131	Improving InSAR geodesy using Global Atmospheric Models. Journal of Geophysical Research: Solid Earth, 2014, 119, 2324-2341.	3.4	220
132	Kinematic model of crustal deformation of Fenwei basin, China based on GPS observations. Journal of Geodynamics, 2014, 75, 1-8.	1.6	39
133	Evaluating sub-pixel offset techniques as an alternative to D-InSAR for monitoring episodic landslide movements in vegetated terrain. Remote Sensing of Environment, 2014, 147, 133-144.	11.0	134
134	Land subsidence in southwest Cyprus revealed from C-band radar interferometry. , 2014, , .		2
135	Validating Accuracy of Rayleigh-Wave Dispersion Extracted from Ambient Seismic Noise Via Comparison with Data from a Ground-Truth Earthquake. Bulletin of the Seismological Society of America, 2014, 104, 2133-2141.	2.3	6
136	Rapid strain accumulation on the Ashkabad fault (Turkmenistan) from atmosphereâ€corrected InSAR. Journal of Geophysical Research: Solid Earth, 2013, 118, 3674-3690.	3.4	57
137	Using advanced InSAR time series techniques to monitor landslide movements in Badong of the Three Gorges region, China. International Journal of Applied Earth Observation and Geoinformation, 2013, 21, 253-264.	2.8	105
138	Rupture history of the 2010 Ms 7.1 Yushu earthquake by joint inversion of teleseismic data and InSAR measurements. Tectonophysics, 2013, 584, 129-137.	2.2	13
139	Kinematic fault slip evolution source models of the 2008 M7.9 Wenchuan earthquake in China from SAR interferometry, GPS and teleseismic analysis and implications for Longmen Shan tectonics. Geophysical Journal International, 2013, 194, 1138-1166.	2.4	97
140	Evaluation of ASTER GDEM using GPS benchmarks and SRTM in China. International Journal of Remote Sensing, 2013, 34, 1744-1771.	2.9	82
141	The 2011 MW 6.8 Burma earthquake: fault constraints provided by multiple SAR techniques. Geophysical Journal International, 2013, 195, 650-660.	2.4	71
142	Postseismic motion after the 2001 M _W 7.8 Kokoxili earthquake in Tibet observed by InSAR time series. Journal of Geophysical Research, 2012, 117, .	3.3	67
143	Contemporary uplift of the Sierra Nevada, western United States, from GPS and InSAR measurements. Geology, 2012, 40, 667-670.	4.4	51
144	Slip in the 2010–2011 Canterbury earthquakes, New Zealand. Journal of Geophysical Research, 2012, 117, .	3.3	103

#	Article	IF	CITATIONS
145	MERIS Atmospheric Water Vapor Correction Model for Wide Swath Interferometric Synthetic Aperture Radar. IEEE Geoscience and Remote Sensing Letters, 2012, 9, 257-261.	3.1	12
146	Study and Establishment of Regional Elastic Block Strain Model Based on GPS data. Lecture Notes in Electrical Engineering, 2012, , 267-275.	0.4	0
147	Imaging ionospheric inhomogeneities using spaceborne synthetic aperture radar. Journal of Geophysical Research, 2011, 116, n/a-n/a.	3.3	57
148	The 2010 <i>M</i> _{<i>W</i>} 6.8 Yushu (Qinghai, China) earthquake: Constraints provided by InSAR and body wave seismology. Journal of Geophysical Research, 2011, 116, .	3.3	84
149	Interseismic slip rate of the Garze–Yushu fault belt in the Tibetan Plateau from C-band InSAR observations between 2003 and 2010. Advances in Space Research, 2011, 48, 2005-2015.	2.6	17
150	Earthquake source parameters of the 2009MW7.8 Fiordland (New Zealand) earthquake from L-band InSAR observations. Earthquake Science, 2011, 24, 199-206.	0.9	0
151	Fault Geometry and Slip Distribution of the 2010 Yushu Earthquakes Inferred from InSAR Measurement. Bulletin of the Seismological Society of America, 2011, 101, 1951-1958.	2.3	18
152	Analysis of Present Tectonic Stress and Regional Ground Fissure Formation Mechanism of the Weihe Basin. Survey Review, 2011, 43, 382-389.	1.2	13
153	Extension on the Tibetan plateau: recent normal faulting measured by InSAR and body wave seismology. Geophysical Journal International, 2010, 183, 503-535.	2.4	146
154	Applying the Coulomb failure function with an optimally oriented plane to the 2008 Mw 7.9 Wenchuan earthquake triggering. Tectonophysics, 2010, 491, 119-126.	2.2	38
155	Using small baseline Interferometric SAR to map nonlinear ground motion: a case study in Northern Tibet. Journal of Applied Geodesy, 2009, 3, .	1.1	3
156	Integration of InSAR Time-Series Analysis and Water-Vapor Correction for Mapping Postseismic Motion After the 2003 Bam (Iran) Earthquake. IEEE Transactions on Geoscience and Remote Sensing, 2009, 47, 3220-3230.	6.3	88
157	Advanced InSAR atmospheric correction: MERIS/MODIS combination and stacked water vapour models. International Journal of Remote Sensing, 2009, 30, 3343-3363.	2.9	119
158	Partial rupture of a locked patch of the Sumatra megathrust during the 2007 earthquake sequence. Nature, 2008, 456, 631-635.	27.8	308
159	The 1998 <i>M</i> _{<i>w</i>} 5.7 Zhangbeiâ€Shangyi (China) earthquake revisited: A buried thrust fault revealed with interferometric synthetic aperture radar. Geochemistry, Geophysics, Geosystems, 2008, 9, .	2.5	24
160	Application of DInSAR-GPS Optimization for Derivation of Fine-Scale Surface Motion Maps of Southern California. IEEE Transactions on Geoscience and Remote Sensing, 2007, 45, 512-521.	6.3	76
161	Interferometric synthetic aperture radar atmospheric correction: Medium Resolution Imaging Spectrometer and Advanced Synthetic Aperture Radar integration. Geophysical Research Letters, 2006, 33, .	4.0	78
162	Interferometric synthetic aperture radar atmospheric correction: GPS topography-dependent turbulence model. Journal of Geophysical Research, 2006, 111, n/a-n/a.	3.3	120

#	Article	IF	CITATIONS
163	A study on the applicability of repeatâ€pass SAR interferometry for generating DEMs over several Indian test sites. International Journal of Remote Sensing, 2006, 27, 595-616.	2.9	16
164	Assessment of the potential of MERIS nearâ€infrared water vapour products to correct ASAR interferometric measurements. International Journal of Remote Sensing, 2006, 27, 349-365.	2.9	83
165	Interferometric synthetic aperture radar (InSAR) atmospheric correction: CPS, Moderate Resolution Imaging Spectroradiometer (MODIS), and InSAR integration. Journal of Geophysical Research, 2005, 110,	3.3	146
166	Comparison of precipitable water vapor derived from radiosonde, GPS, and Moderate-Resolution Imaging Spectroradiometer measurements. Journal of Geophysical Research, 2003, 108, .	3.3	209
167	CPS automatic monitoring system for outside deformation of Geheyan Dam on the Qingjiang River. Geo-Spatial Information Science, 2000, 3, 58-64.	5.3	8
168	Measuring mining induced subsidence with InSAR. , 0, , .		3
169	The 2009 L'Aquila <italic>M</italic> _W 6.3 earthquake: a new technique to locate the hypocentre in the joint inversion of earthquake rupture process. Geophysical Journal International, 0, , .	2.4	16
170	POTENTIAL LANDSLIDE EARLY DETECTION NEAR WENCHUAN BY A QUALITATIVELY MULTI-BASELINE DINSAR METHOD. International Archives of the Photogrammetry, Remote Sensing and Spatial Information Sciences - ISPRS Archives, 0, XLII-3, 253-256.	0.2	2
171	TOWARDS INSAR EVERYWHERE, ALL THE TIME, WITH SENTINEL-1. International Archives of the Photogrammetry, Remote Sensing and Spatial Information Sciences - ISPRS Archives, 0, XLI-B4, 763-766.	0.2	13
172	MERGING DIGITAL SURFACE MODELS IMPLEMENTING BAYESIAN APPROACHES. International Archives of the Photogrammetry, Remote Sensing and Spatial Information Sciences - ISPRS Archives, 0, XLI-B7, 711-718.	0.2	1
173	General Survey of Large-scale Land Subsidence by GACOS-Corrected InSAR Stacking: Case Study in North China Plain. Proceedings of the International Association of Hydrological Sciences, 0, 382, 213-218.	1.0	9
174	TOWARDS INSAR EVERYWHERE, ALL THE TIME, WITH SENTINEL-1. International Archives of the Photogrammetry, Remote Sensing and Spatial Information Sciences - ISPRS Archives, 0, XLI-B4, 763-766.	0.2	3
175	RESEARCH ON THE CRUSTAL DEFORMATION CHARACTERISTICS IN BEIJING USING INSAR AND GNSS TECHNOLOGY. International Archives of the Photogrammetry, Remote Sensing and Spatial Information Sciences - ISPRS Archives, 0, XLII-3, 559-564.	0.2	1
176	RADAR REMOTE SENSING APPLICATIONS IN LANDSLIDE MONITORING WITH MULTI-PLATFORM INSAR OBSERVATIONS: A CASE STUDY FROM CHINA. International Archives of the Photogrammetry, Remote Sensing and Spatial Information Sciences - ISPRS Archives, 0, XLII-2/W13, 1939-1943.	0.2	1
177	DEFORMATION MONITORING OF HIGH-LATITUDE PERMAFROST REGION OF NORTHEASTERN CHINA WITH TIME SERIES INSAR TECHNIQUE. International Archives of the Photogrammetry, Remote Sensing and Spatial Information Sciences - ISPRS Archives, 0, XLII-2/W13, 1777-1780.	0.2	1
178	CHARACTERIZATION OF THE FROST HEAVE DEFORMATIONS IN HIGH LATITUDE AND DEEP SEASONALLY FROZEN SOIL OF INNER MONGOLIA WITH SENTINEL-1 INSAR OBSERVATIONS. International Archives of the Photogrammetry, Remote Sensing and Spatial Information Sciences - ISPRS Archives, 0, XLIII-B3-2020, 887-891.	0.2	0
179	Coastal Lowlands' Inundation Risk Assessment with High-resolution TanDEM-X DEM in Qingdao Coastal Plains, China. Proceedings of the International Association of Hydrological Sciences, 0, 382, 621-627.	1.0	0
180	Topographic insights in the Frome-Callabonna system and the elevation of a newly surveyed highstand shoreline. Transactions of the Royal Society of South Australia, 0, , 1-19.	0.4	1